Chemical Science

ROYAL SOCIETY OF CHEMISTRY

EDGE ARTICLE

View Article Online
View Journal | View Issue

Cite this: *Chem. Sci.*, 2025, **16**, 18844

All publication charges for this article have been paid for by the Royal Society of Chemistry

Accelerated intersystem crossing enhances NIR emission in $Au_{52}(SR)_{32}$ nanoclusters by surface ligand engineering

Linlin Zeng, [a] Yitong Wang, [b] Junjun Tan,[c] Quanbing Pei,[a] Jie Kong, [a] Wei Zhang, [a] Shuji Ye, [a] Rongchao Jin,*[b] Yi Luo *[ac] and Meng Zhou *[a]

Received 28th May 2025
Accepted 9th September 2025

DOI: 10.1039/d5sc03898g

rsc.li/chemical-science

Surface ligand modification is an effective strategy for enhancing the photoluminescence (PL) of atomically precise gold nanoclusters. Nevertheless, the underlying mechanism of PL enhancement, particularly the role of triplet states remains vague. In this work, we picture the formation and relaxation of triplet states in a series of four $Au_{52}(SR)_{32}$ nanoclusters with different –R groups by probing their excited state dynamics. Electronic pump–probe spectroscopy reveals that the nanoclusters with fewer methyl groups on the ligand exhibit a faster intersystem crossing (ISC) pathway, hence boosting the triplet-state-related emission. Additionally, the metal core of the four nanoclusters exhibits similar low-frequency vibrations, suggesting that the variation in non-radiative relaxation is primarily mediated by ligand vibrations, rather than the metal core vibrations. These findings establish that ligand-induced PL enhancement is driven by both accelerated ISC and reduced vibrational dissipation. This work sheds light on the mechanism by which ligand engineering enhances PL in gold nanoclusters, highlighting the critical role of triplet state dynamics in tailoring their emission properties, which hold promise in applications such as sensing, bioimaging, optoelectronics, and solar energy conversion.

Introduction

Atomically precise gold nanoclusters, consisting of a central gold core and surface-protecting ligands, exhibit unique and intriguing photoluminescence (PL) properties.[1,2] Their moderate energy gaps (0.5–2 eV) enable highly desirable near-infrared (NIR) emission,[2] making them promising candidates for applications in biological imaging, optoelectronic devices and sensitizers.[3–10] However, according to the energy gap law, the non-radiative relaxation rate increases as the energy gap decreases, resulting in relatively low NIR photoluminescence quantum yields (PLQYs).[11] To enhance the PLQY of gold nanoclusters, considerable efforts have focused on increasing radiative rates and suppressing non-radiative relaxation. Increasing the rigidity of protecting ligands and heteroatom doping have emerged as two key strategies to enhance PL.[2,12] For instance, the emission intensity of $Au_{22}(SG)_{18}$ increased nine-fold upon binding tetraoctylammonium (TOA) cations to the glutathione anion ligands, which effectively rigidified the ligand shell.[13] Similarly, Au_{13} clusters protected by rigid N-heterocyclic carbene (NHC) ligands exhibited higher PLQYs compared to those protected by phosphine ligands.[14] As for heteroatom doping, a notable example is the silver-doped, rod-shaped $Ag_{13}Au_{12}$ cluster, which achieved a remarkable PLQY increase to 40.1%, far surpassing its undoped rod-shaped Au_{25} counterpart.[15,16] Recently, Shi *et al.* reported that replacing six gold atoms with copper in $Au_{22}(^{t}BuPhC{\equiv}C)_{18}$ enabled near unity NIR luminescence.[17] Additionally, bisNHC ligands incorporating naphthalene linkers have been found to enhance Au_{13} PL through strong CH–π interactions that increase the ligand rigidity.[18] While these strategies have demonstrated significant improvements in PL, their underlying mechanisms remain only partially understood. The existing explanations largely attribute PL enhancement to suppressed non-radiative decay *via* ligand rigidification or modified electronic structures *via* doping,[2] yet the role of excited state dynamics in governing the emission efficiency is often overlooked.

With deeper insights into origins and mechanisms of PL in gold nanoclusters, triplet excited states may serve as key intermediates. Experiments involving triplet energy transfer (TET) and triplet–triplet annihilation upconversion have demonstrated that metal nanoclusters can efficiently populate triplet excited states and exhibit room-temperature phosphorescence.[7,8,19–21] This underscores the need to consider triplet state dynamics when designing strategies to enhance PL. With this perspective, two fundamental questions

[a]*Hefei National Research Center for Physical Sciences at the Microscale, University of Science and Technology of China, Hefei, Anhui 230026, P. R. China. E-mail: yiluo@ustc.edu.cn; mzhou88@ustc.edu.cn*

[b]*Department of Chemistry, Carnegie Mellon University, Pittsburgh, Pennsylvania 15213, USA. E-mail: rongchao@andrew.cmu.edu*

[c]*Hefei National Laboratory, University of Science and Technology of China, Hefei, Anhui 230088, China*

arise: (1) Is ligand-induced PL enhancement solely a consequence of suppressed non-radiative relaxation through increased rigidity? (2) What role do triplet state formation and relaxation play in ligand-induced PL enhancement?

In this work, we choose a series of four $Au_{52}(SR)_{32}$ nanoclusters with an identical metal core but different thiolate ligands (*i.e.*, different substituents on the aromatic –SPh ligand) as a platform to explore the mechanism by which ligands regulate PL enhancement. By employing ultrafast transient absorption spectroscopy, we probed the triplet state dynamics and coherent oscillation of the gold core. Our results reveal that the intersystem crossing (ISC) rate plays a crucial role in PL enhancement of $Au_{52}(SR)_{32}$: nanoclusters exhibiting the strongest NIR emission predominantly populate the T_1 state through a faster ISC pathway. Furthermore, modifications to the carbon tails of the ligands have a negligible effect on the core vibrations. This work illustrates the important role of both efficient ISC and suppressed ligand vibration in enhancing the PL of metal nanoclusters, offering new insights into the fundamentals of ligand-regulated luminescence.

Results and discussion

Fig. 1A shows the $Au_{52}S_{32}$ framework of $Au_{52}(SR)_{32}$ and the four distinct thiolate ligands. $Au_{52}(SR)_{32}$ has an Au_{32} core, surrounded by four $Au(SR)_2$ staples along the midsection and eight $Au_2(SR)_3$ staples attached to the top and bottom.[22,23] The UV-vis absorption spectra of all $Au_{52}(SR)_{32}$ in toluene solution display two characteristic peaks near 400 and 800 nm (Fig. 1B), consistent with the pervious study.[22] Photoluminescence measurements of the four $Au_{52}(SR)_{32}$ nanoclusters in toluene under ambient conditions reveal near-infrared emission above 900 nm (Fig. 1C, colored profiles). Among these nanoclusters, $Au_{52}(p\text{-MBT})_{32}$ exhibits the highest PL intensity, and the PLQY decreases in the order: $Au_{52}(p\text{-MBT})_{32}$ > $Au_{52}(4\text{-EBT})_{32}$ > $Au_{52}(\text{-IPBT})_{32}$ > $Au_{52}(TBBT)_{32}$.[22] In addition to solution-phase studies, we also investigated $Au_{52}(SR)_{32}$ embedded in poly(methyl methacrylate) (PMMA) films. The absorption and PL properties of $Au_{52}(SR)_{32}$ films (Fig. 1B and C, black profiles) closely resemble those observed in toluene. Furthermore, these nanoclusters exhibit higher PLQY in films compared to solutions.[22]

To explore the evolution of excited states of $Au_{52}(SR)_{32}$ nanoclusters, nanosecond transient absorption (ns-TA) experiments were first conducted. The ns-TA data maps show a broad excited-state absorption (ESA) signal spanning 450–700 nm, and a prominent ground-state bleaching (GSB) signal at ~800 nm, which aligns well with the absorption peak in the steady-state UV-vis spectra (Fig. 2A and S1A–C). Only a long-lived excited-state is observed in ns-TA. By fitting the kinetic trace at 562 nm, the excited-state lifetime was determined (Fig. 2B, S1D–F and Table S1). $Au_{52}(p\text{-MBT})_{32}$ exhibits the longest excited-state lifetime of 604 ns, while $Au_{52}(TBBT)_{32}$ has the shortest lifetime of 145 ns. For comparison, the PL lifetimes of $Au_{52}(SR)_{32}$ in toluene under ambient conditions were also measured by time-correlated single photon counting (TCSPC) (Fig. 2C and S2). Both the TA and PL lifetimes decrease progressively as the number of $-CH_3$ on the carbon tail increases. In addition, the excited-state lifetimes obtained from ns-TA and PL measurements are comparable (Fig. 2D), indicating that the excited-state observed in ns-TA is the origin of the PL emission in $Au_{52}(SR)_{32}$.

Ligand-protected metal nanoclusters have emerged as novel triplet sensitizers for photon upconversion,[24–28] primarily due to their ability to readily populate triplet excited-states facilitated by strong spin–orbit coupling (SOC). In the previous report,[22] the singlet oxygen emission at 1274 nm was observed when $Au_{52}(SR)_{32}$ solutions were purged with O_2, which occurs through energy transfer from $Au_{52}(SR)_{32}$ triplet states to O_2 (triplet ground state), resulting in singlet O_2 (excited state) and then phosphorescence emission at 1274 nm. Additionally, an abnormal and non-monotonic blue shift of the $Au_{52}(SR)_{32}$ emission peak was detected as the temperature decreased.[22] These findings confirmed that both phosphorescence and thermally activated delayed fluorescence (TADF) coexist in the PL of $Au_{52}(SR)_{32}$. Here, we further investigate the triplet-state-

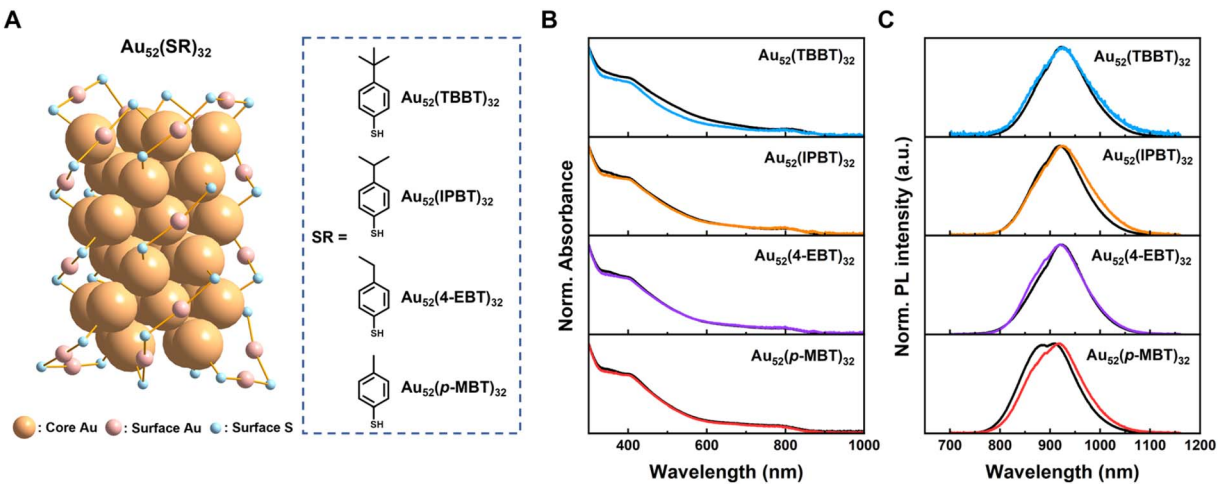

Fig. 1 (A) The structure of $Au_{52}(SR)_{32}$ and the four different thiolate ligands. (B) Normalized UV-vis spectra of the four $Au_{52}(SR)_{32}$ nanoclusters in toluene (colored lines) and in PMMA films (black lines). (C) Normalized PL spectra of the four $Au_{52}(SR)_{32}$ in toluene (colored lines) and in PMMA films (black lines) under 650 nm excitation.

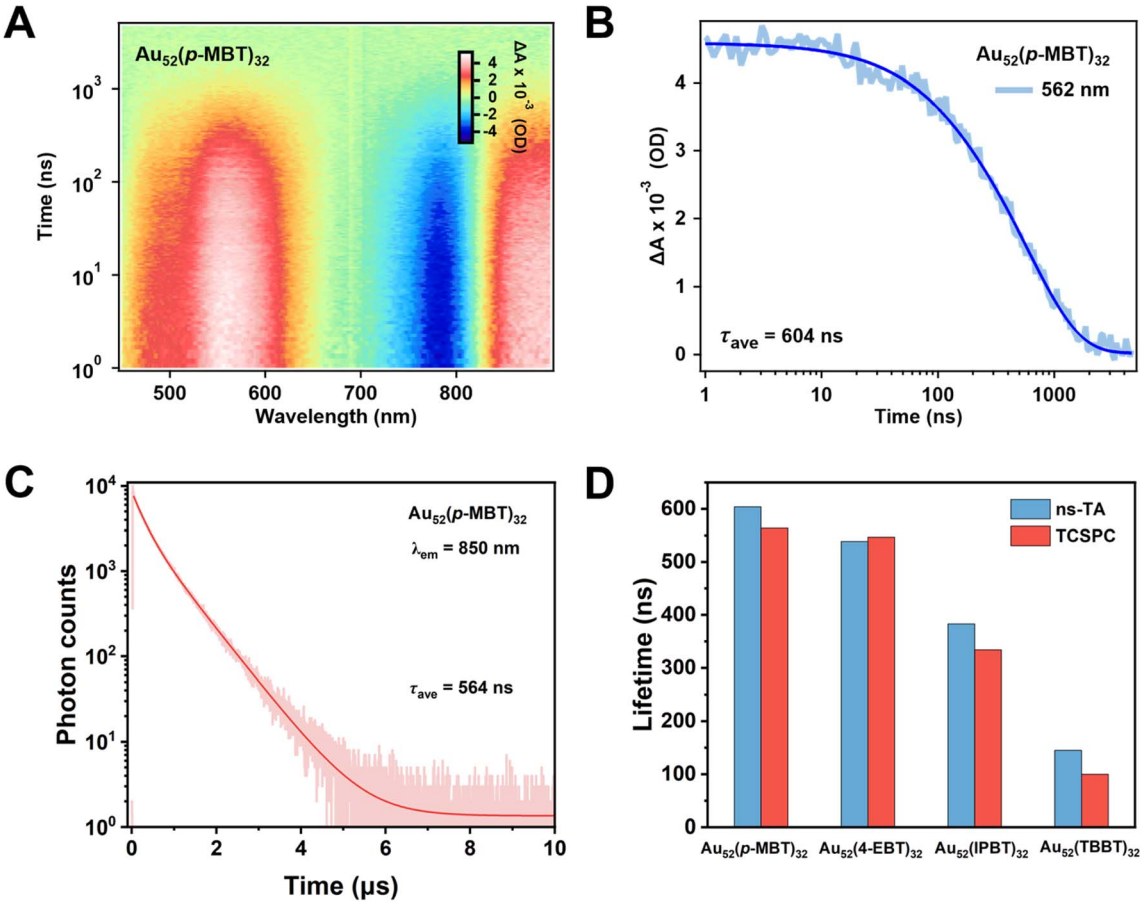

Fig. 2 (A) Ns-TA data map of $Au_{52}(p\text{-MBT})_{32}$ in toluene with 400 nm excitation. (B) TA kinetic trace and corresponding fit at 562 nm. (C) PL decay trace and fitting of $Au_{52}(p\text{-MBT})_{32}$ in toluene at 850 nm under ambient conditions (λ_{ex} = 375 nm). (D) Comparison of the excited-state lifetimes derived from ns-TA and PL measurements.

related emission in $Au_{52}(p\text{-MBT})_{32}$ through TET experiments. The UV-vis absorption spectra of mixed $Au_{52}(p\text{-MBT})_{32}$ and rubrene in solutions are shown in Fig. 3A. No new absorption peaks were observed with the addition of rubrene, ruling out the formation of a ground-state complex between clusters and rubrene. As the rubrene concentration increased, the PL lifetime of $Au_{52}(SR)_{32}$ decreased (Fig. 3B). The data fit well with the linear Stern–Volmer equation, indicating that the PL quenching of the clusters occurs through collisional interactions with rubrene.[29] This PL quenching is attributed to TET from $Au_{52}(SR)_{32}$ to rubrene during collisions, with a determined TET rate constant of 2.1×10^8 M^{-1} s^{-1}. The successful observation of TET in $Au_{52}(p\text{-MBT})_{32}$ provides direct evidence for the phosphorescence of $Au_{52}(SR)_{32}$.

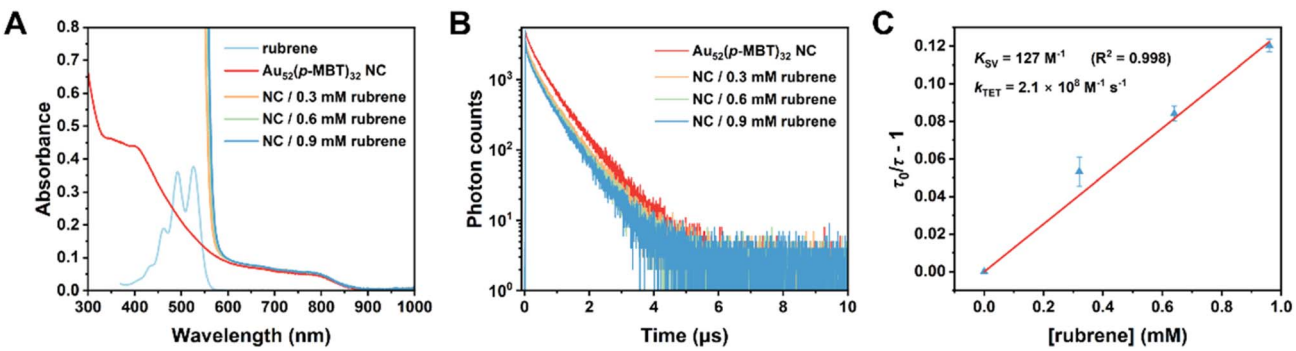

Fig. 3 (A) UV-vis spectra of $Au_{52}(p\text{-MBT})_{32}$, rubrene and $Au_{52}(p\text{-MBT})_{32}$/rubrene mixed solutions. (B) PL decay traces of $Au_{52}(p\text{-MBT})_{32}$ and $Au_{52}(p\text{-MBT})_{32}$/rubrene mixed solutions at 850 nm under a N_2 atmosphere. (C) Stern–Volmer plot of PL lifetimes of $Au_{52}(p\text{-MBT})_{32}$ at varying rubrene concentrations.

Modifying ligands on $Au_{52}(SR)_{32}$ significantly influences their triplet excited state emission. $Au_{52}(p\text{-MBT})_{32}$ exhibits a PLQY of 18.3%, whereas $Au_{52}(TBBT)_{32}$ shows a much lower PLQY of 3.8%.[22] The intersystem crossing from singlet to triplet states plays a critical role in facilitating triplet excited state emission, and may account for the large differences in PLQY among the $Au_{52}(SR)_{32}$ nanoclusters. To investigate ISC in these clusters, femtosecond TA (fs-TA) spectroscopy was employed to further probe their excited-state dynamics. Upon excitation of $Au_{52}(SR)_{32}$ at 380 nm, an initial broad ESA signal spanning the entire probe wavelength range was observed, with two peaks at ~550 and ~700 nm (Fig. S3 and S4). At a delay time of approximately 1 ns, the ESA signal became narrower and the ESA signal intensity above 650 nm decreased significantly. The change of TA spectral profiles suggests that a state-to-state evolution occurred. Kinetic traces probed at ~600 nm revealed a rapid decay within the first 1 ps, corresponding to this excited-state evolution (Fig. 4A). In contrast, when pumped at 800 nm, the relatively narrow ESA signal appeared instantaneously, and the broad ESA observed with 380 nm excitation was absent (Fig. S5). Furthermore, kinetic traces probed at ~600 nm did not exhibit the fast decay (Fig. 4B). Since excitation at 800 nm corresponds to near-bandgap excitation and directly populates the lower excited-state, the fast ESA decay can be attributed to the internal conversion (IC) from a higher excited-state to a lower excited-state.

An evident slow rise in the ESA signal within 100 ps, following the rapid IC, was observed in the excited-state dynamics of $Au_{52}(SR)_{32}$ nanoclusters. After 100 ps, the ESA signal intensity remained constant throughout the measured time range (Fig. 4A). The long-lived excited-state, which does not decay within the fs-TA measurement window, corresponds to the emissive triplet excited-state identified in ns-TA. Thus, the slow rise in ESA is attributed to ISC. Interestingly, the amplitude of this rise (Fig. 4A) correlates well with the PLQY of the various $Au_{52}(SR)_{32}$ nanoclusters by an inverse relationship, that is, $Au_{52}(p\text{-MBT})_{32}$, which exhibits the highest PLQY, shows the least observable rise in its kinetic trace (Fig. 4A), whereas the other three nanoclusters with lower PLQYs display more and more pronounced rise amplitudes. The time constant of the ISC is about 11 ps (Table S2). However, under 800 nm excitation, all four nanoclusters exhibit a slow rise in the ESA signal (Fig. 4B and Table S3). This suggests that the involvement of higher excited-states (S_n, T_n) is pivotal in facilitating the ISC process. A similar phenomenon has been reported in other metal clusters.[25,27,30,31] In Au_{13} nanoclusters, negligible SOC exists between S_1 and T_1 according to the El-Sayed rule (*i.e.*, a change in orbital type for achieving stronger ISC).[32] However, large SOC matrix

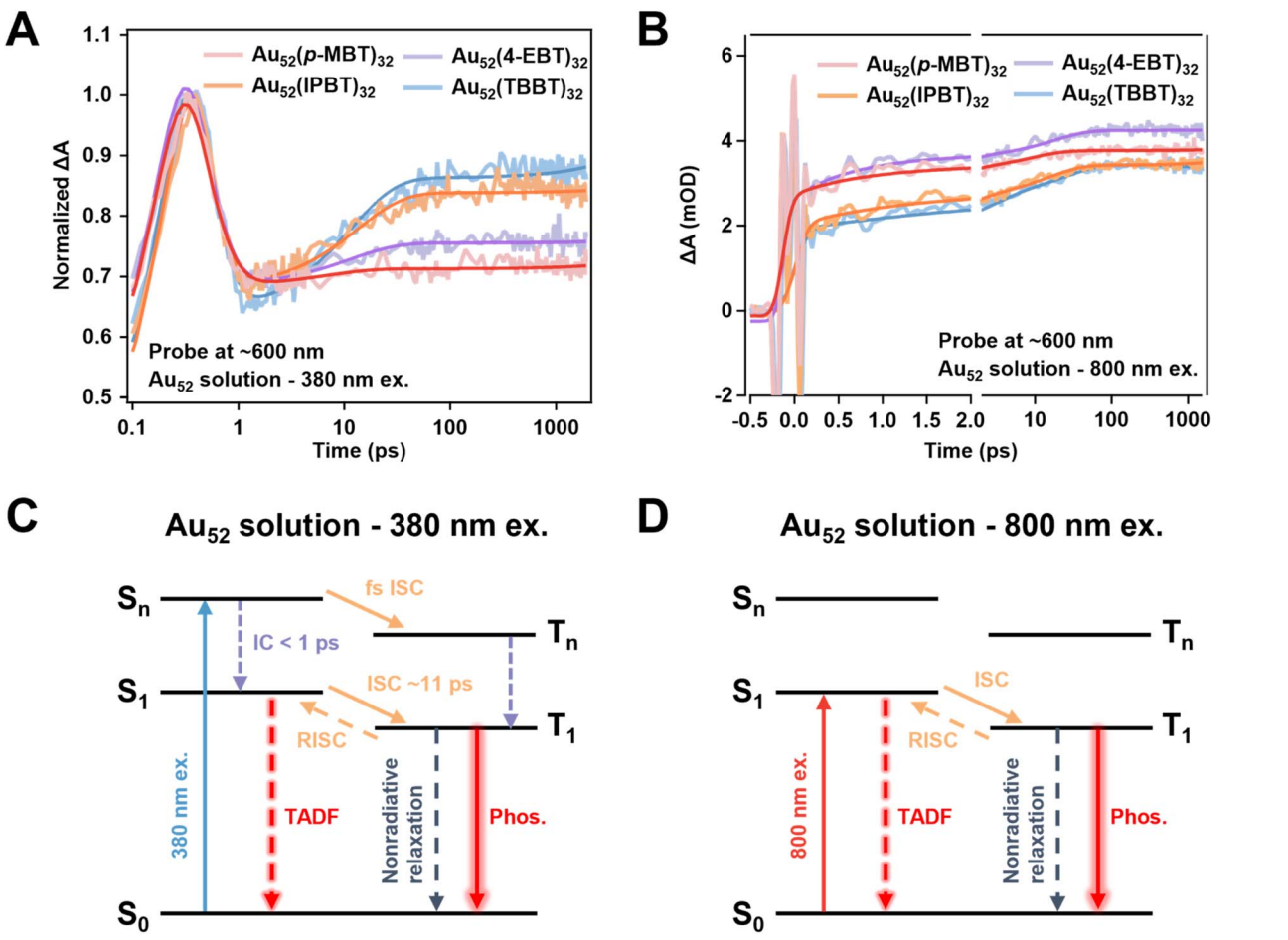

Fig. 4 Fs-TA kinetic traces and corresponding fits at ~600 nm for $Au_{52}(SR)_{32}$ in toluene under 380 nm (A) and 800 nm (B) excitation. Proposed photoluminescence mechanism for $Au_{52}(SR)_{32}$ in toluene under 380 nm (C) and 800 nm (D) excitation.

elements between S_1 and higher triplet excited-states (*e.g.*, T_2, T_3, T_4) contribute to the ultrafast and near-unity ISC.[25] In isomeric $Au_{28}(CHT)_{20}$ clusters (where CHT denotes cyclohexanethiolate), the ISC rate from S_1 to T_2 is several orders of magnitude faster than from S_1 to T_1, with T_2 serving as a critical intermediate for excited-state relaxation.[30] For the rise observed in $Au_{52}(SR)_{32}$ fs-TA dynamics, we ascribe it to a direct ISC process from S_1 to T_1. With near-bandgap excitation, the nanoclusters are directly excited to S_1 and subsequently undergo ISC to T_1, resulting in the observed rise in all four nanoclusters (Fig. 4D). In contrast, with 380 nm excitation, the nanoclusters are initially populated in higher singlet excited-states (S_n), which rapidly undergo IC to S_1, but for $Au_{52}(p\text{-MBT})_{32}$, ultrafast ISC from S_n to T_n may occur, which was not captured by our fs-TA (time resolution ~ 100 fs). For the other three nanoclusters, the ISC process (~11 ps) primarily occurs between S_1 and T_1, leading to the observed rise in their TA kinetic traces (Fig. 4C). As the proportion of the picosecond ISC pathway increases, the PLQY of $Au_{52}(SR)_{32}$ progressively decreases.

When these four $Au_{52}(SR)_{32}$ nanoclusters were embedded in PMMA films, both their excited-state lifetimes (Figure S7) and PLQYs were significantly increased compared to those in solutions.[22] To understand the origin of PL enhancement, we further investigated the excited-state dynamics of the nanoclusters in films. The fs-TA data maps of $Au_{52}(SR)_{32}$ films exhibited spectral features similar to those observed in toluene solutions, including a broad ESA signal with peak around 550 nm (Fig. 5A and S6A–C). However, the dynamics of $Au_{52}(SR)_{32}$ films were distinctly different (Fig. 5B) compared to solutions. For instance, $Au_{52}(TBBT)_{32}$ showed the most pronounced ESA rise in toluene (1–100 ps), but no such distinct slow rise was observed in the film. This absence of rise indicates that the ISC from S_1 to T_1 occurs much more rapidly in the film than in the solution. Theoretically, the ISC rate can be expressed using first-order perturbation theory:[33,34]

$$k_{ISC} = \frac{2\pi}{\hbar}|V|^2\rho$$

where $V = \langle\Psi_S|\hat{H}_{SO}|\Psi_T\rangle$ represents the SOC between the singlet and triplet states, and ρ is the Frank–Condon weighted density of states. In the high temperature limit, ρ can be written as:[34]

$$\rho = \frac{1}{\sqrt{4\pi k_B T}}\exp\left[-\frac{(\Delta E+\lambda)^2}{4\lambda k_B T}\right]$$

where ΔE is the energy gap between the singlet and triplet states, and λ is the reorganization energy. In the PMMA film environment, the better alignment of energy levels between S_1 and T_1 reduces the energy gap ΔE, facilitating both ISC and reverse intersystem crossing (RISC), thus enhancing the PLQY.[35,36] Additionally, the SOC may be enhanced in the film, further contributing to faster ISC observed in the solid state (Fig. 5C).[37]

The emission mechanism of $Au_{52}(SR)_{32}$ is strongly associated with triplet states. For metal nanoclusters involving TADF, the strong SOC induces ultrafast ISC (10^{-15} to 10^{-12} s), leading to a rapid equilibrium between the S_1 and T_1 states before emission occurs.[38] Notably, the ISC dynamics observed in our transient absorption measurements already indicate the establishment of this equilibrium. Consequently, faster ISC not only increases the triplet state population but also accelerates the S_1–T_1 equilibration, thereby facilitating both phosphorescence and TADF.

The fewer methyl groups present on the ligand, the stronger the restriction on its motion.[22] The correlation between ligand flexibility, ISC dynamics and PLQY observed in $Au_{52}(SR)_{32}$ nanoclusters reveals an important structure–property relationship. However, whether the general trend—that more flexible ligands lead to slower ISC and consequently reduced PLQY—can be extended to other metal nanoclusters requires further studies. Differences in core structure and ligand–metal interactions may result in distinct excited-state behaviors. Therefore, while our findings provide valuable insights, further investigations on a broader range of ligand-protected nanoclusters will be necessary to establish the universality of this mechanism.

A broadband laser pulse can not only populate electronic excited-states but also induce superpositions of vibrational states, resulting in coherent vibrational wavepackets.[39–44] These wavepackets manifest as periodic oscillatory modulation in the amplitude of pump–probe signals.[45] As shown in Fig. 6A and S8, the early-time TA maps of $Au_{52}(SR)_{32}$ films display clear oscillatory modulations across the entire ESA region. To determine the frequency of the coherent vibrational motion, we performed fast Fourier transformation (FFT) on the pure oscillation

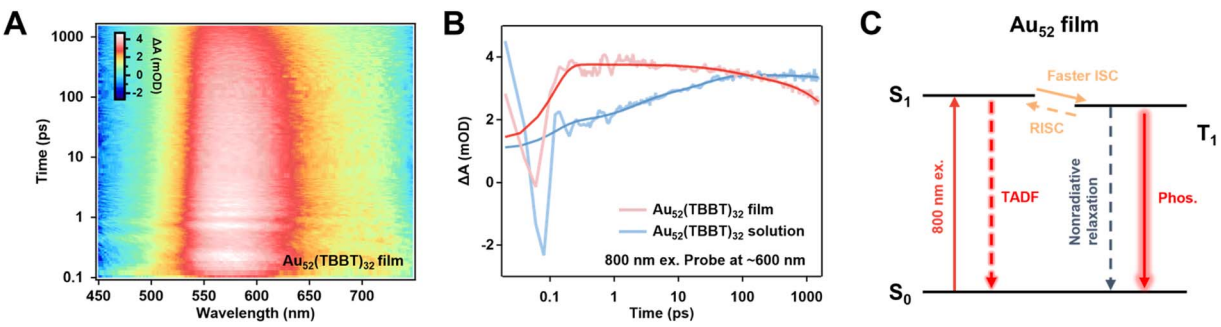

Fig. 5 (A) Fs-TA data map of $Au_{52}(TBBT)_{32}$ film under 800 nm excitation. (B) Comparison of fs-TA kinetic traces and corresponding fits at 600 nm for $Au_{52}(TBBT)_{32}$ in solution and in film. (C) Proposed photoluminescence mechanism for $Au_{52}(SR)_{32}$ film under 800 nm excitation.

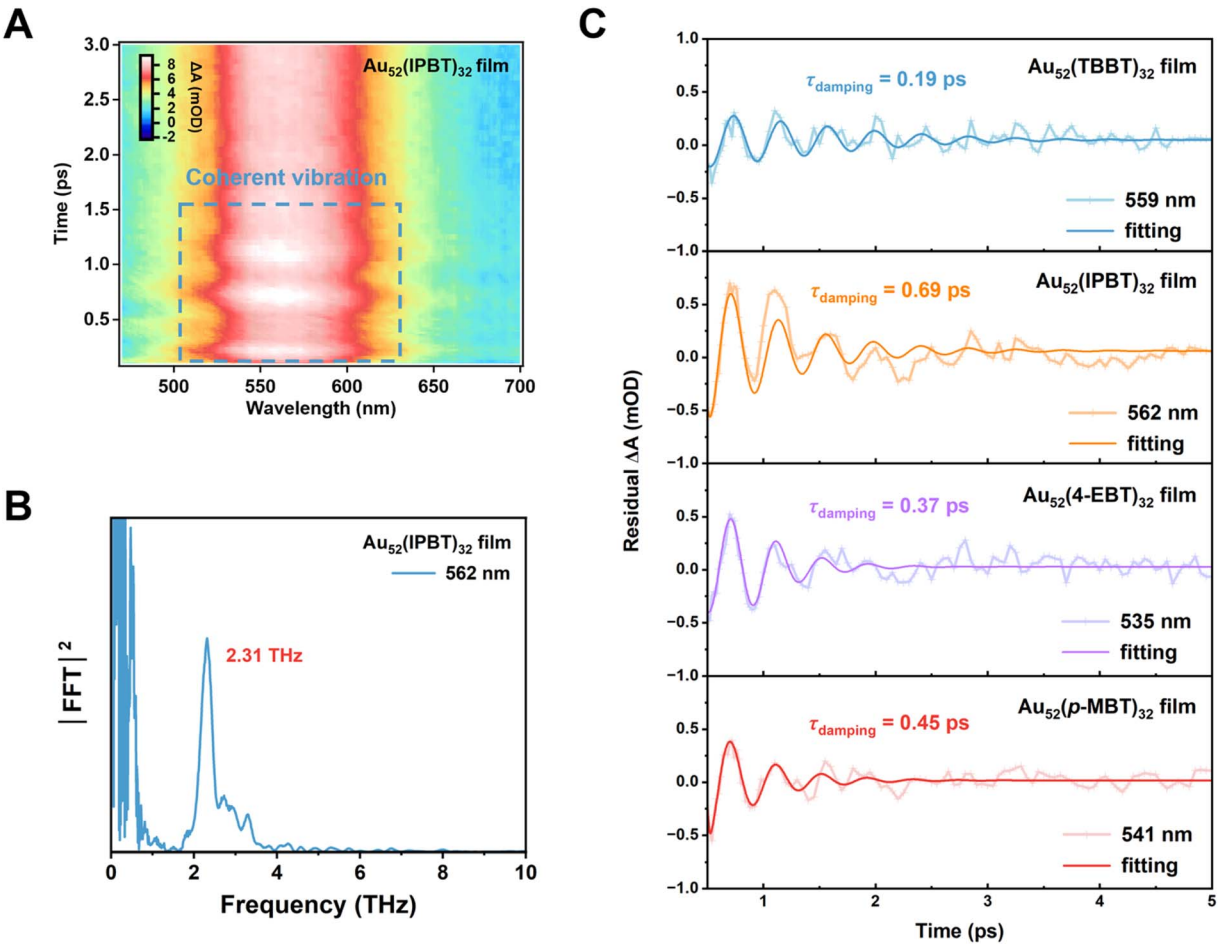

Fig. 6 (A) Fs-TA data map of $Au_{52}(IPBT)_{32}$ film within the first 3 ps upon 800 nm excitation. (B) FFT analysis of the kinetic trace at 562 nm. (C) Oscillation dynamics and the corresponding fits.

signals, which were obtained by subtracting the excited-state population dynamics (Fig. S9). The FFT analysis reveals a dominant frequency of ~2.4 THz (80 cm^{-1}) for all four $Au_{52}(SR)_{32}$ nanoclusters (Fig. 6B and S10). Since these oscillations appear in the ESA signals, the ~2.4 THz wavepacket motion is attributed to vibrations on the potential energy surface of the excited electronic state.

Low-frequency coherent vibrations in metal nanoclusters are typically associated with the acoustic vibrations of the metal core.[46–52] In spherical Au_{25} and Ag_{44} clusters, a similar oscillation frequency (~2.4 THz) had been observed and assigned to the breathing mode, characterized by symmetric, in-phase radical oscillations of the metal atoms.[46,51,53] Accordingly, the 2.4 THz vibration mode observed in $Au_{52}(SR)_{32}$ nanoclusters herein should be attributed to the breathing mode of the gold core. The similarity in coherent vibration frequency in these four $Au_{52}(SR)_{32}$ suggests that their metal cores share a similar structure, consistent with the X-ray crystallographic results.[22] The damping dynamics of the coherent vibrations were extracted by fitting the residual oscillations with exponentially decaying cosine functions (Fig. 6C). The oscillation period was ~0.4 ps for all $Au_{52}(SR)_{32}$ nanoclusters, consistent with the vibrational frequencies (~2.4 THz) obtained from FFT analysis (Table S4). The damping time constants ranged from 0.19 to 0.69 ps. A previous report on Au_{10} nanoclusters highlighted that the rigidity of surface ligands can influence the metal core vibrations, hence, reducing the amplitude of acoustic vibrations and enhancing the core structural relaxation time in electronic dynamics.[54] This suppression leads to enhanced PL due to reduced non-radiative relaxation caused by core structural changes. In contrast, such a suppression of coherent vibration amplitude or damping time was not observed in the $Au_{52}(SR)_{32}$ nanoclusters, although the reduction of methyl groups restricted surface ligand motions.[22] This finding indicates that the rigidity of surface ligands has a negligible effect on the metal core vibrations of $Au_{52}(SR)_{32}$. Instead, non-radiative relaxation may be predominantly mediated by the high-frequency vibrational and rotational motions of the surface thiolate ligands.

Conclusion

In summary, this study elucidates that the impact of ligand modifications on the ISC governs the PL properties of $Au_{52}(SR)_{32}$ nanoclusters. By selecting a model system with an identical metal core but distinct thiolate ligands, we have systematically

studied how ligand modifications influence the excited-state dynamics. TA results demonstrate that ligand variations significantly impact the ISC channels in $Au_{52}(SR)_{32}$. For the $Au_{52}(p\text{-MBT})_{32}$ nanoclusters, a stronger SOC likely exists between high-lying singlet and triplet states (S_n and T_n), facilitating a faster ISC on the femtosecond scale. This highly efficient ISC pathway promotes the population of the triplet excited-state, leading to higher PLQY. In contrast, for the other three clusters, the ISC predominantly occurs from S_1 to T_1. This slower ISC process results in lower PLQYs compared to $Au_{52}(p\text{-MBT})_{32}$. Furthermore, while all four nanoclusters exhibit similar core vibrational frequencies, their non-radiative relaxation primarily occurs through ligand vibrations, and the suppression of these vibrations further enhances PLQY. These findings provide a refined mechanistic framework for understanding ligand-induced PL enhancement in metal nanoclusters.

Author contributions

L. Z. performed the spectral experiments and data analysis. Y. W. synthesized and characterized the metal nanoclusters. J. T., Q. P., J. K., W. Z. and S. Y. helped in the spectral measurements. L. Z. and M. Z. wrote the manuscript. R. J., Y. L. and M. Z. designed the project and revised the manuscript. All authors approved the final version of the manuscript.

Conflicts of interest

Authors declare that they have no conflict of interest.

Data availability

Data for this article are available from the corresponding authors upon reasonable request.

The data supporting this article have been included as part of the SI. Supplementary information: Materials and methods, SI Text, Fig. S1–S13, Tables S1–S4. See DOI: **https://doi.org/10.1039/d5sc03898g**.

Acknowledgements

MZ acknowledges the financial support from the Strategic Priority Research Program of the Chinese Academy of Sciences (XDB0450202), National Natural Science Foundation of China (22273095) and Chinese Academy of Sciences (YSBR-007).

References

1 R. Jin, C. Zeng, M. Zhou and Y. Chen, *Chem. Rev.*, 2016, **116**, 10346–10413.
2 Z. Liu, L. Luo and R. Jin, *Adv. Mater.*, 2024, **36**, 2309073.
3 A. Baghdasaryan, F. Wang, F. Ren, Z. Ma, J. Li, X. Zhou, L. Grigoryan, C. Xu and H. Dai, *Nat. Commun.*, 2022, **13**, 5613.
4 H. Liu, G. Hong, Z. Luo, J. Chen, J. Chang, M. Gong, H. He, J. Yang, X. Yuan, L. Li, X. Mu, J. Wang, W. Mi, J. Luo, J. Xie and X.-D. Zhang, *Adv. Mater.*, 2019, **31**, 1901015.
5 X.-H. Ma, J. Li, P. Luo, J.-H. Hu, Z. Han, X.-Y. Dong, G. Xie and S.-Q. Zang, *Nat. Commun.*, 2023, **14**, 4121.
6 B. Niesen and B. P. Rand, *Adv. Mater.*, 2014, **26**, 1446–1449.
7 D. Arima and M. Mitsui, *J. Am. Chem. Soc.*, 2023, **145**, 6994–7004.
8 D. Arima, S. Hidaka, S. Yokomori, Y. Niihori, Y. Negishi, R. Oyaizu, T. Yoshinami, K. Kobayashi and M. Mitsui, *J. Am. Chem. Soc.*, 2024, **146**, 16630–16638.
9 Y. Xiao, Z. Wu, Q. Yao and J. Xie, *Aggregate*, 2021, **2**, 114–132.
10 W. Zhang, T. Xu, Y. Chen, G. Zhang and Y. Song, *Polyoxometalates*, 2025, **4**, 9140082.
11 R. Englman and J. Jortner, *Mol. Phys.*, 1970, **18**, 145–164.
12 H. Lin, X. Song, O. J. H. Chai, Q. Yao, H. Yang and J. Xie, *Adv. Mater.*, 2024, **36**, 2401002.
13 K. Pyo, V. D. Thanthirige, K. Kwak, P. Pandurangan, G. Ramakrishna and D. Lee, *J. Am. Chem. Soc.*, 2015, **137**, 8244–8250.
14 M. R. Narouz, S. Takano, P. A. Lummis, T. I. Levchenko, A. Nazemi, S. Kaappa, S. Malola, G. Yousefalizadeh, L. A. Calhoun, K. G. Stamplecoskie, H. Häkkinen, T. Tsukuda and C. M. Crudden, *J. Am. Chem. Soc.*, 2019, **141**, 14997–15002.
15 S. Wang, X. Meng, A. Das, T. Li, Y. Song, T. Cao, X. Zhu, M. Zhu and R. Jin, *Angew. Chem., Int. Ed.*, 2014, **53**, 2376–2380.
16 Q. Li, C. J. Zeman IV, Z. Ma, G. C. Schatz and X. W. Gu, *Small*, 2021, **17**, 2007992.
17 W.-Q. Shi, L. Zeng, R.-L. He, X.-S. Han, Z.-J. Guan, M. Zhou and Q.-M. Wang, *Science*, 2024, **383**, 326–330.
18 V. K. Kulkarni, E. L. Albright, E. Zeinizade, E. Steele, J. Chen, L. Ding, S. Malola, S. Takano, K. Harrington, N. Kwon, T. I. Levchenko, M. Nambo, T. Tsukuda, H. Häkkinen, K. Stamplecoskie, G. Zheng and C. M. Crudden, *J. Am. Chem. Soc.*, 2025, **147**, 4017–4025.
19 M. Mitsui, *J. Phys. Chem. Lett.*, 2024, **15**, 12257–12268.
20 L. Zeng, W.-Q. Shi, J. Kong, W. Zhang, Q.-M. Wang, Y. Luo and M. Zhou, *Adv. Opt. Mater.*, 2025, **13**, 2402991.
21 W.-Q. Shi, L. Zeng, Z.-C. Long, Z.-J. Guan, X.-S. Han, F. Hu, M. Zhou and Q.-M. Wang, *J. Phys. Chem. Lett.*, 2025, **16**, 2204–2211.
22 Y. Wang, Z. Liu, A. Mazumder, C. G. Gianopoulos, K. Kirschbaum, L. A. Peteanu and R. Jin, *J. Am. Chem. Soc.*, 2023, **145**, 26328–26338.
23 C. Zeng, Y. Chen, C. Liu, K. Nobusada, N. L. Rosi and R. Jin, *Sci. Adv.*, 2015, **1**, e1500425.
24 Y. Niihori, Y. Wada and M. Mitsui, *Angew. Chem., Int. Ed.*, 2021, **60**, 2822–2827.
25 K. Yoshida, D. Arima and M. Mitsui, *J. Phys. Chem. Lett.*, 2023, **14**, 10967–10973.
26 M. Mitsui, Y. Miyoshi and D. Arima, *Nanoscale*, 2024, **16**, 14757–14765.
27 M. Mitsui and A. Uchida, *Nanoscale*, 2024, **16**, 3053–3060.
28 Y. Niihori, T. Kosaka and Y. Negishi, *Mater. Horiz.*, 2024, **11**, 2304–2322.

29 *Principles of Fluorescence Spectroscopy*, ed. J. R. Lakowicz, Springer US, Boston, MA, 2006, pp. 277–330.
30 A. Mazumder, K. Li, Z. Liu, Y. Wang, Y. Pei, L. A. Peteanu and R. Jin, *ACS Nano*, 2024, **18**, 21534–21543.
31 C. Zhu, J. Xin, J. Li, H. Li, X. Kang, Y. Pei and M. Zhu, *Angew. Chem., Int. Ed.*, 2022, **61**, e202205947.
32 M. A. El-Sayed, *J. Chem. Phys.*, 1963, **38**, 2834–2838.
33 S. S. Murali, J. K. Gallaher, C. Janiseck, E. J. Tay, I. Wagner, K. E. Thorn, A. Ilina, R. R. Tamming, J. Wang, C. Sester, J. J. Sutton, M. B. Price, K. C. Gordon, K. Chen, X. Zhan, J. M. Hodgkiss and P. A. Hume, *J. Am. Chem. Soc.*, 2023, **145**, 732–744.
34 T. J. Penfold, E. Gindensperger, C. Daniel and C. M. Marian, *Chem. Rev.*, 2018, **118**, 6975–7025.
35 Z. Liu, L. Luo, J. Kong, E. Kahng, M. Zhou and R. Jin, *Nanoscale*, 2024, **16**, 7419–7426.
36 L. Luo, Z. Liu, X. Du and R. Jin, *J. Am. Chem. Soc.*, 2022, **144**, 19243–19247.
37 W. Zhang, S. Li, Y. Gong, J. Zhang, Y. Zhou, J. Kong, H. Fu and M. Zhou, *Angew. Chem., Int. Ed.*, 2024, **63**, e202404978.
38 T.-Y. Li, S.-J. Zheng, P. I. Djurovich and M. E. Thompson, *Chem. Rev.*, 2024, **124**, 4332–4392.
39 S. R. Rather and G. D. Scholes, *J. Phys. Chem. A*, 2016, **120**, 6792–6799.
40 P. Kim, A. J. S. Valentine, S. Roy, A. W. Mills, A. Chakraborty, F. N. Castellano, X. Li and L. X. Chen, *J. Phys. Chem. Lett.*, 2021, **12**, 6794–6803.
41 S. R. Rather, G. D. Scholes and L. X. Chen, *Acc. Chem. Res.*, 2024, **57**, 2620–2630.
42 Y.-C. Wei, B.-H. Chen, R.-S. Ye, H.-W. Huang, J.-X. Su, C.-Y. Lin, J. Hodgkiss, L.-Y. Hsu, Y. Chi, K. Chen, C.-H. Lu, S.-D. Yang and P.-T. Chou, *Angew. Chem., Int. Ed.*, 2023, **62**, e202300815.
43 C. Wright and G. V. Hartland, *Annu. Rev. Phys. Chem.*, 2025, **76**, 57–81.
44 M. Zhou, C. Zeng, Y. Song, J. W. Padelford, G. Wang, M. Y. Sfeir, T. Higaki and R. Jin, *Angew. Chem., Int. Ed.*, 2017, **56**, 16257–16261.
45 S. R. Rather, N. P. Weingartz, S. Kromer, F. N. Castellano and L. X. Chen, *Nature*, 2023, **620**, 776–781.
46 H. Qian, M. Y. Sfeir and R. Jin, *J. Phys. Chem. C*, 2010, **114**, 19935–19940.
47 M. Y. Sfeir, H. Qian, K. Nobusada and R. Jin, *J. Phys. Chem. C*, 2011, **115**, 6200–6207.
48 M. Zhou, S. Tian, C. Zeng, M. Y. Sfeir, Z. Wu and R. Jin, *J. Phys. Chem. C*, 2017, **121**, 10686–10693.
49 M. Zhou, R. Jin, M. Y. Sfeir, Y. Chen, Y. Song and R. Jin, *Proc. Natl. Acad. Sci. U. S. A.*, 2017, **114**, E4697–E4705.
50 W. Zhang, J. Kong, Y. Li, Z. Kuang, H. Wang and M. Zhou, *Chem. Sci.*, 2022, **13**, 8124–8130.
51 J. Kong, Z. Kuang, W. Zhang, Y. Song, G. Yao, C. Zhang, H. Wang, Y. Luo and M. Zhou, *Chem. Sci.*, 2024, **15**, 6906–6915.
52 X. Yu, W. Pei, W.-w. Xu, Y. Zhao, Y. Su and J. Zhao, *Inorg. Chem.*, 2023, **62**, 20450–20457.
53 P. Maioli, T. Stoll, H. E. Sauceda, I. Valencia, A. Demessence, F. Bertorelle, A. Crut, F. Vallée, I. L. Garzón, G. Cerullo and N. Del Fatti, *Nano Lett.*, 2018, **18**, 6842–6849.
54 Y. Zhong, J. Zhang, T. Li, W. Xu, Q. Yao, M. Lu, X. Bai, Z. Wu, J. Xie and Y. Zhang, *Nat. Commun.*, 2023, **14**, 658.